Discovery and Preclinical Profiling of 3-[4-(Morpholin-4-yl)-7H-pyrrolo[2,3-d]pyrimidin-5-yl]benzonitrile (PF-06447475), a Highly Potent, Selective, Brain Penetrant, and in Vivo Active LRRK2 Kinase Inhibitor

Jaclyn L. Henderson,[†] Bethany L. Kormos,[†] Matthew M. Hayward,[∥] Karen J. Coffman,[∥] Jayasankar Jasti,[∥] Ravi G. Kurumbail,[∥] Travis T. Wager,[†] Patrick R. Verhoest,[†] G. Stephen Noell,[⊥] Yi Chen,[‡] Elie Needle,[‡] Zdenek Berger,[‡] Stefanus J. Steyn,[§] Christopher Houle,[#] Warren D. Hirst,[‡] and Paul Galatsis*,[†]

[†]Worldwide Medicinal Chemistry, [‡]Neuroscience Research Unit, and [§]Pharmacokinetics, Dynamics, and Metabolism, Pfizer Worldwide R&D, 610 Main Street, Cambridge, Massachusetts 02139, United States

[∥]Worldwide Medicinal Chemistry, [⊥]Primary Pharmacology Group, and [#]Drug Safety R&D, Pfizer Worldwide R&D, Eastern Point Road Groton, Connecticut 06340, United States

S *Supporting Information*

ABSTRACT: Leucine rich repeat kinase 2 (LRRK2) has been genetically linked to Parkinson's disease (PD) by genome-wide association studies (GWAS). The most common LRRK2 mutation, G2019S, which is relatively rare in the total population, gives rise to increased kinase activity. As such, LRRK2 kinase inhibitors are potentially useful in the treatment of PD. We herein disclose the discovery and optimization of a novel series of potent LRRK2 inhibitors, focusing on improving kinome selectivity using a surrogate crystallography approach. This resulted in the identification of **14** (PF-06447475), a highly potent, brain penetrant and selective LRRK2 inhibitor which has been further profiled in in vivo safety and pharmacodynamic studies.
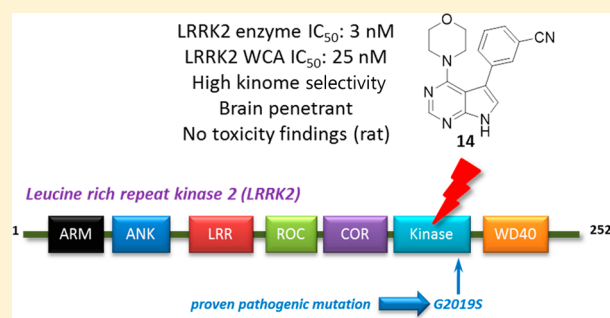
INTRODUCTION

Parkinson's disease (PD) is a debilitating neurodegenerative disorder that affects over seven million people worldwide. Despite extensive research, the underlying disease mechanisms, and thus targets for therapeutic intervention, have remained unclear.[1] Recent genome-wide association studies (GWAS) have identified several proteins with significant linkages to PD.[2] Among these, leucine rich repeat kinase 2 (LRRK2) is a highly promising target, as PD patients carrying LRRK2 mutations are almost indistinguishable from idiopathic PD patients, indicating that this may represent a common mechanism between inherited and sporadic PD.[2] Furthermore, a number of additional genetic variants in LRRK2 have been identified as having an increased PD risk, suggesting that it is important in the cause and pathogenesis of PD in a greater proportion of patients with this disease than previously believed.[2]

While there is growing evidence to support a central role of LRRK2 dysfunction/dysregulation in the development of PD, the complexity of LRRK2 has made elucidation of its (patho)physiological role challenging.[3] For example, the natural substrates of the kinase and the protein-binding partners have remained elusive. Nevertheless, the potential for disease modification and the recent successes in the development of kinase inhibitors for chronic illness have attracted the attention of the pharmaceutical industry, resulting in the discovery of a number of LRRK2 inhibitors[4] with a range of CNS druglike properties[5,6] (Figure 1). Although the kinase domain of LRRK2 shares low overall sequence homology with other kinases, it has been characterized as a serine−threonine kinase in the TKL group of kinases and has highest homology to LRRK1 and the receptor-interacting protein (RIP) kinases.[3a,5] Because of the chronic nature of PD and the aging patient population, an excellent safety profile, potentially requiring a high degree of kinase selectivity, is critical for a successful therapy in this area. In this report we describe the discovery and optimization of a series of pyrrolopyrimidines leading to a highly selective and brain penetrant compound, which has proved to be a useful tool in interrogating both central and peripheral LRRK2 biology.

RESULTS AND DISCUSSION

Our initial strategy was to conduct a high throughput screen (HTS) of the Wyeth compound file using truncated, GST-
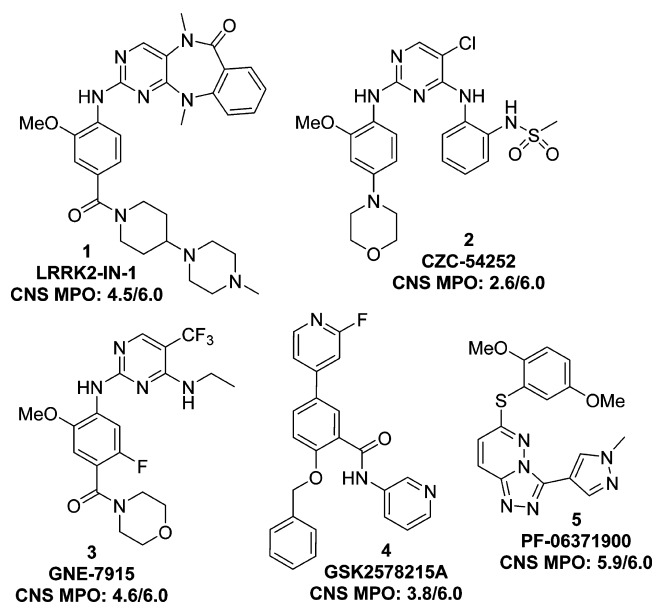
Figure 1. Previously published LRRK2 inhibitors highlighting CNS druglike scores[5] (CNS druglike space: CNS MPO ≥ 4.0/6.0).

tagged LRRK2 protein and LRRKtide as a surrogate kinase substrate in a FRET assay. This resulted in a relatively large number of hits (0.6% confirmed hits) which featured known ATP hinge-binding scaffolds. Thus, a kinase selectivity panel (KSS) was used in conjunction with ligand efficiency (LE), lipophilic efficiency (LipE), and CNS desirability multi-parameter optimization scores (CNS MPO)[5] to triage the initial hits. Because of its small size, high LE, and excellent selectivity profile, imidazopyrimidine **6** stood out as a key hit of this preliminary triage. Instead of running a second HTS to interrogate the Pfizer compound file, we used a selection of diverse hits from the Wyeth screen as templates to identify additional chemical matter from a set of compounds derived from (1) our internal kinase-targeted library,[7] (2) compounds that had activity in kinases with similar ATP-binding sites as determined by alignment in PFAAT,[8] and (3) virtual screening based on similarity determined by atom-pairs[9] and feature trees.[10] On the basis of the original imidazopyrimidine hit **6**, highly potent pyrrolopyrimidine **7** was identified (Figure 2). While this compound does have affinity for several other kinases, the overall selectivity profile was considered acceptable
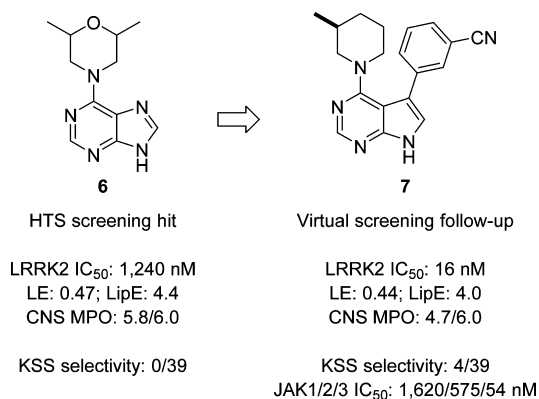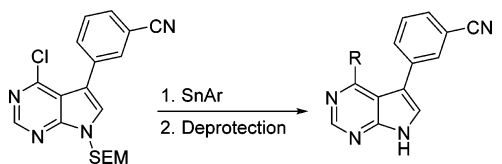
because of its enhanced LRRK2 potency, and thus, further optimization was initiated.
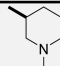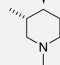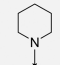
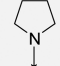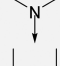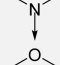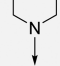Lead compound **7** originated from a previous program targeting the Janus kinase (JAK) family, and thus, crystal structures of related compounds were available in house. It is interesting to note that others have also identified lead matter for their LRRK2 programs from JAK inhibitors,[11] perhaps confirming this family as a suitable surrogate in the absence of LRRK2 crystallographic data. The available crystal structures and literature data suggested the pyrrolopyrimidine was likely an ATP-binding pocket two-point hinge binder, with the aryl moiety oriented toward the DFG motif and the amine occupying the ATP-ribose pocket. Synthetically, this hit offered opportunities for parallel medicinal chemistry optimization with the amine installation proceeding from the pyrimidyl chloride through an S_NAr reaction and the aryl group being accessed through Suzuki cross-coupling reactions. Initial optimization focused on improving both kinase selectivity and human liver microsome (HLM) stability through optimization of the lipophilic 3-methylpiperidine, summarized in Table 1. All compounds prepared were predicted to be in good CNS druglike space (CNS MPO[5]) and exhibited passive permeability and P-gp efflux ratios congruent with high brain availability.

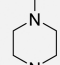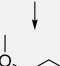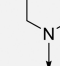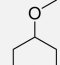Although initial library work investigated a diverse set of both primary and secondary amines, simple cyclic and acyclic secondary amines proved optimal for LRRK2 potency. From lead compound **7**, it was found that the methyl group on the amine substituent was not a requirement for activity, with piperidine **9** and pyrrolidine **10** being close to equipotent. Despite its small size, dimethylamino substitution (**12**) was one of the more potent compounds, with reduced lipophilicity affording improved clearance. Interestingly, azetidine analogue **11** lost 10× to 20× LRRK2 potency compared to the closely related analogues **10** and **12**, a finding that may be due to an overall electronic effect on the core hinge-binding interaction. Attempts to add additional polarity to the molecule were not well tolerated; basic amines such as piperazine **15** ameliorated LRRK2 potency, while ethers **16−18** failed to improve either potency or microsomal stability. Morpholine **14** was the exception, showing improvements in potency, clearance, and selectivity over the piperidine analogues.

After this single round of optimization, we felt that both dimethylamino **12** and morpholino **14** analogues were sufficiently potent in the LRRK2 whole cell assay (WCA) (pS935 end point) to warrant additional profiling. In particular, we were interested in corroborating what at the time was a relatively new assay by generating a second measure of LRRK2 potency in a physiologically relevant system.[12] Testing these two compounds in human PBMC lysates using the ActivX KiNativ technology gave both an indication of LRRK2 potency alongside a much wider selectivity assessment.[13] While LRRK2 inhibition lined up well with the WCA (ActivX LRRK2 IC_{50}: **12**, 42 nM; **14**, 15 nM), the selectivity profile of **14** particularly differentiated it from the dimethylamino analogue (Figure 3 and Supporting Information for further details, Figure S1 and Table S2). Of particular note in the off-target activity profiles were the numerous hits from the STE20 kinase family (LOK, SLK, and MST kinases) and the observation that, despite their resemblance to previously reported JAK inhibitors, both compounds were devoid of JAK activity.

In an effort to identify key opportunities to enhance selectivity and to drive further understanding of LRRK2

Figure 2. Initial HTS hit leading to identification of pyrrolopyrimidine scaffold.

Table 1. SAR around 3-Methylpiperidine[e]

CMPD	R	WT LRRK2 IC$_{50}$ (nM)[a]	G2019S IC$_{50}$ (nM)[a]	LRRK2 WCA IC$_{50}$ (nM)[b]	HLM CL (mL/min/kg)[c]	KSS Selectivity[d]
7		16	49	210	220	4/39
8		69	171	1,579	204	6/39
9		6	28	182	131	7/39
10		8	64	432	63	5/39
11		115	325	7,687	21	nt
12		5	15	89	70	6/39
13		20	151	443	114	3/39
14		3	11	25	36	3/39
15		1,830	5,223	nt	20	nt
16		79	154	nt	208	3/39
17		393	950	nt	nt	nt
18		95	219	nt	>300	nt

[a]Biochemical assay, geometric mean ($n \geq 2$). [b]Cellular assay, geometric mean ($n \geq 2$). [c]Human liver microsomal clearance. [d]Pfizer internal kinase selectivity panel, quoted as number of kinases displaying >50% inhibition at 1 μM. [e]nt: not tested.

binding interactions in the absence of a LRRK2 X-ray crystal structure, we employed a surrogate crystallography approach based on kinase similarity and crossover of compound activity. LRRK2 only has ∼30% residue identity and ∼50% residue similarity in the kinase domain compared to its closest neighbors; however, its ATP-binding site residues have greater similarity to other kinases. For example, mammalian STE20-like protein kinase 3 (MST3) ATP-binding site residues are 73% similar to those in LRRK2. As such, it was not surprising that there was some off-target activity at the MST family of kinases (vide infra) suggesting MST3 was a reasonable surrogate crystallographic system for LRRK2.

As mentioned, the pyrrolopyrimidine scaffold is a well-known two-point hinge binder in kinases, and this was confirmed by the X-ray crystal structure of **14** with MST3 (Figure 4). The pyrrole NH formed a H-bond (HB) with the backbone carbonyl of Glu85, and N1 formed a HB with the backbone NH of Leu87 (corresponding to Glu1948 and Ala1950 in LRRK2, respectively). N3 was involved in a water-mediated HB network to the backbone carbonyl of Leu87 and the side chain of Asp94, which correspond to Ala1950 and Arg1957 in LRRK2, respectively. The morpholine ring formed van der Waals (VDW) interactions with the Gly-rich loop, including Ile15, Gly16, Lys17, and Val23 (corresponding to Leu1885, Gly1886, Asp1887, and Val1893 in LRRK2), and the oxygen of
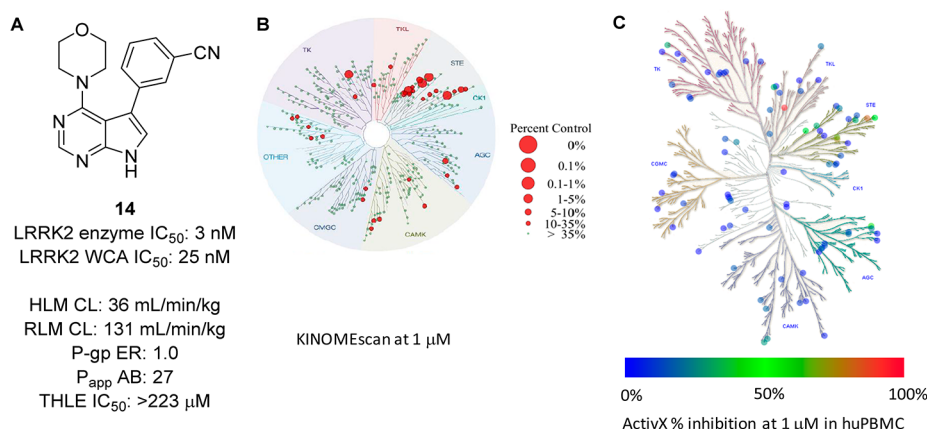
Figure 3. Detailed profiling of **14**: (A) potency and ADMET; (B) in vitro kinase selectivity (DiscoveRx KINOMEscan); (C) ex vivo kinase selectivity (ActivX KiNativ).
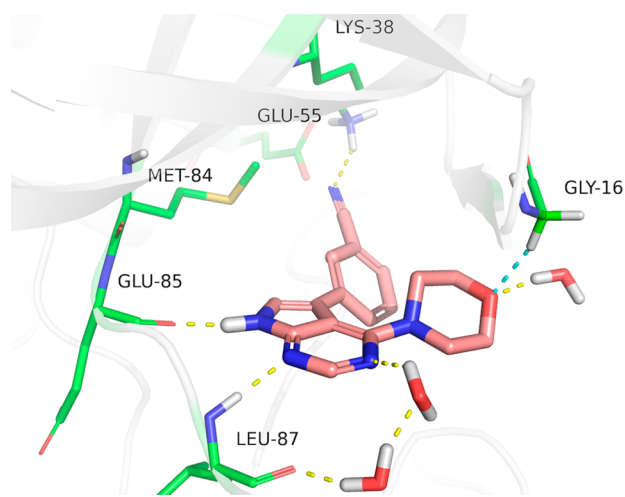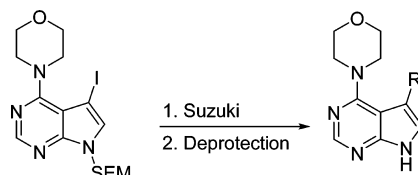

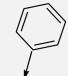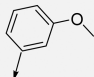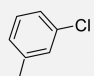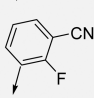**Figure 4.** X-ray crystal structure of **14** with MST3 (1.63 Å, PDB code 4U8Z).
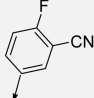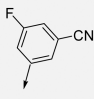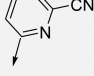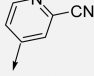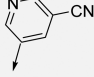
the morpholine ring was in position to make a nontraditional CH···O HB to Gly16. Such an interaction may contribute to the modest boost in LRRK2 potency observed with the change from piperidine **9** to morpholine **14** in this position.

As shown in Table 2, attempts to optimize the 3-cyanophenyl substituent illustrated the important contribution of this part of the molecule to both potency and selectivity. In the X-ray crystal structure of **14** with MST3 (Figure 4), the nitrile formed a charge-assisted HB with the conserved Lys38 (Lys1906 in LRRK2), which maintained its salt bridge with Glu55 (Glu1920 in LRRK2) from the αC-helix. The phenyl ring formed VDW interactions with the ceiling and floor of the binding site. A comparison of **14** and **19** suggested the nitrile interaction contributes a 3× to 4× potency improvement in LRRK2. Surprisingly for an interaction with a residue that is conserved across the kinome, it also appeared to be contributing to enhanced selectivity. It has been shown in other chemotypes that it is possible to modulate kinase binding affinity and selectivity by varying steric and electrostatic properties of substituents in this region despite the highly conserved Lys residue.[14] SAR efforts also indicated that the interactions of this portion of the molecule with LRRK2 are quite sensitive to both steric and electronic effects. An ortho-F substituent in the 2-position of the aryl ring was tolerated by

LRRK2 (**22**), although this small change reduced selectivity; however, addition of fluoro substitutions at other positions around the ring significantly reduced LRRK2 potency (**23** and **24**), illustrating the compact nature of this pocket. In an attempt to lower HLM clearance, we examined the effects of various heterocycles both with and without the 3-cyano group. Similar to the fluoro substitution, a pyridyl nitrogen in the 2-position was tolerated in terms of LRRK2 potency (**25**); however, other pyridyl regioisomers were significantly less potent. The position of the nitrogen in the different pyridyl regioisomers did not significantly affect the torsional profile or conformation of the phenyl ring; however, a nitrogen in the 4- or 5-position was oriented toward residues that create a negative electrostatic potential in that part of the pocket (the catalytic Asp147, the backbone carbonyl of Ala133, and the carbonyl of the Asn134 side chain—Asp2017, His1998, and Asn1999 in LRRK2), which may lead to a loss in potency due to electrostatic repulsion. In comparison to the cyanophenyl, a majority of the simple heteroaromatics examined were detrimental to LRRK2 potency with N-methylpyrazole **28** being one of the few analogues that maintained LRRK2 potency while improving human microsomal stability. Although the whole cell potency was somewhat higher than **14**, we felt the KSS selectivity and improved pharmacokinetic properties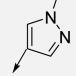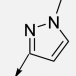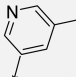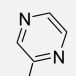 of pyrazole analogue **28** warranted further profiling. The N-methyl group also provided a straightforward opportunity for radiolabeling, which was of particular interest in terms of potential PET ligand development. An ActivX selectivity screen revealed that **28** was around 3× less potent at LRRK2 than **14** (50 nM in ActivX) and shared similarly high selectivity (see Supporting Information, Figure S2 and Tables S1 and S2). Examining the X-ray crystal structure of **28** in MST3 (Figure 5) revealed similar interactions to those seen with **14**, including a water-mediated HB between the pyrazole N and the conserved Lys38 (Lys1906 in LRRK2), mimicking the interaction of the cyanophenyl with this residue. The development of radiolabeled **28** will be disclosed in a subsequent publication (manuscript in preparation).

Because of the lack of information around the role of the MST kinases and any consequences in terms of compound safety profile, we aimed to further optimize **14** to increase selectivity versus this family.[15] Of the residue differences determined by sequence alignment of the ATP binding pockets[16] of LRRK2 and MST1−4 (Figure 6), four were considered as potential areas to target for selectivity. Several of

D

Table 2. SAR around 3-Cyanophenyl[e]

CMPD	R	WT LRRK2 IC$_{50}$ (nM)[a]	G2019S IC$_{50}$ (nM)[a]	LRRK2 WCA IC$_{50}$ (nM)[b]	HLM CL (mL/min/kg)[c]	KSS Selectivity[d]
19		9	14	198	48	10/39
20		28	46	882	135	10/39
21		8	13	144	60	7/39
22		3	9	20	36	8/39
23		117	920	2,460	44	1/39
24		80	688	2,082	24	nt
25		9	26	298	10	1/39
26		686	4,514	nt	<8	nt
27		2,243	6,599	nt	9	0/39
28		12	36	278	<10	2/39
29		53	90	2,570	11	nt
30		18	30	211	69	5/39
31		914	1,199	nt	<8	nt

[a]Biochemical assay, geometric mean ($n \geq 2$). [b]Cellular assay, geometric mean ($n \geq 2$). [c]Human liver microsomal clearance. [d]Pfizer internal kinase selectivity panel quoted as number of kinases displaying >50% inhibition at 1 μM. [e]nt: not tested.

these residues have been targeted previously with different chemotypes to drive LRRK2 selectivity over other kinases.[4d,11,14a,17] Our initial interest was drawn to the arginine residue at H13 (Figure 6),[16] as targeting this residue would be expected to enhance selectivity not only over the MST kinases but also across the kinome because of its low overall incidence at that position: 3% of the kinome has an arginine at H13, while 16% has a positively charged amino acid. An arginine at the H13 position is likely solvent exposed and quite flexible, thus forming a HB or cation−π interaction with a ligand may restrict the motion of the arginine side chain. This would cause a conformational entropic penalty, which could cancel out any gain in binding free energy achieved with a productive interaction. However, interactions of this nature are prece-
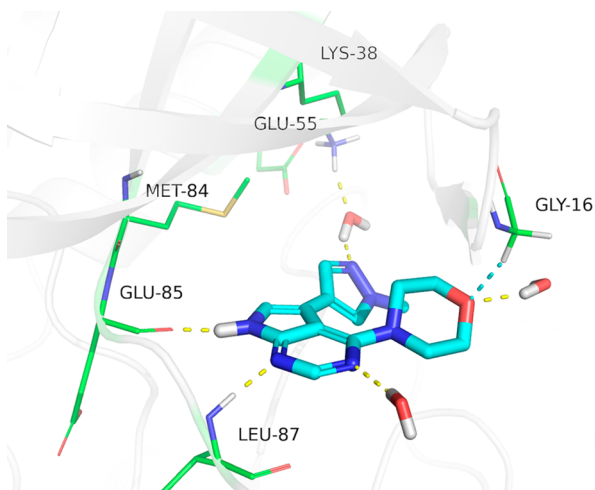
Figure 5. X-ray crystal structure of **28** in MST3 (1.77 Å, PDB code 4W8D).

dented in the literature. For example, in the 1Q4L X-ray crystal structure of GSK-3β,[18a] the inhibitor I-5 forms a HB interaction with Arg141 (H13 residue) through a carboxylate group, and in the 1Q5K X-ray crystal structure of GSK-3β,[18b] the inhibitor AR-A014418 forms a cation−π interaction with Arg141 through a phenyl substituent. In both of these cases, it can be seen that a residue, Glu137, is interacting with Arg141 through a salt bridge, restricting the motion of the arginine and enabling productive interactions with the ligands without paying a large conformational entropic penalty. To assess the flexibility of the H13 arginine in LRRK2, molecular dynamics

(MD) simulations were run on several LRRK2 homology models. On the basis of the results of 10 ns simulations for each homology model (60 ns total), Arg1957 may be involved in HB interactions with nearby residues up to 68% of the simulation time, restricting its motion and possibly orienting it in a position for ligand interaction. Alternatively, it is possible that Arg1957 interacts with one of the other LRRK2 protein domains, which could also restrict its motion. These analyses suggested the possibility that Arg1957 could occupy a position whereby it could form either a HB or cation−π interaction with a substituent occupying the 3-position of the morpholine. We thus embarked on exploring substitution at this position alongside potential morpholine isosteres. A summary of this optimization is provided in Table 3.
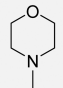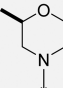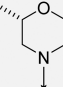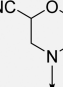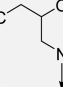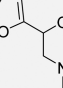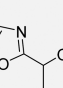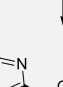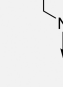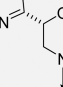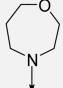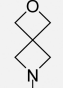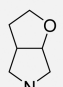
Although **14** had generally good kinome selectivity, there was significant off-target activity against the MST kinases as evidenced by both the enzyme assay and ActivX data. We were surprised to find that addition of a simple methyl group (**33**) increased selectivity for LRRK2 to 25× over MST2, although this was to the slight detriment of LRRK2 potency. Selectivity versus MST4 was much higher than that for MST2 (and MST1; vide infra), which could potentially be explained by the glycine at C1 allowing MST2 a greater degree of conformational flexibility. Polar groups such as nitrile (**34**) or CH$_2$CN (**35**) did not significantly enhance selectivity over the methyl analogue, suggesting that we were unsuccessful in targeting a HB interaction with the arginine in these cases. We also investigated heterocyclic substituents to contact the H13 arginine. Such analogues led to a substantial enhancement in selectivity over MST2, our best example being oxadiazole **38**, which did not significantly lose LRRK2 potency over
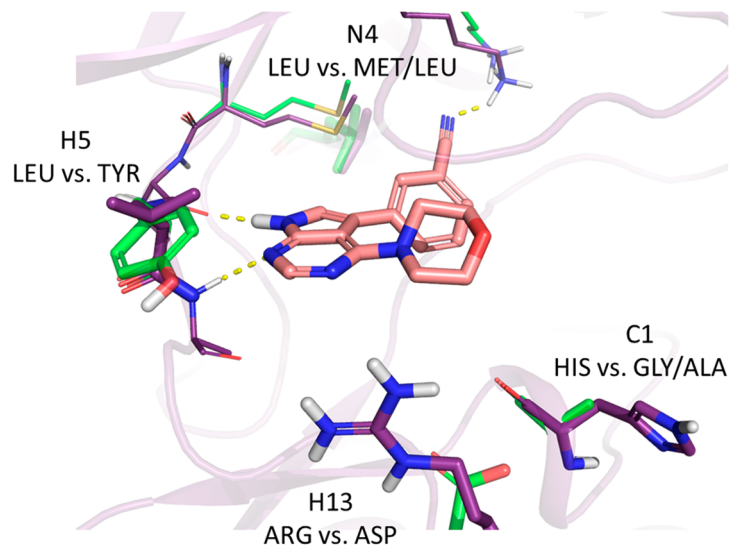
Residue ID/ Kinase	L1	N4	N5	H1	H5	H6	H7	H8	H11	H12	H13	C1	C5	C6	C7	C8
LRRK2	L 1885	L 1924	I 1933	L 1945	L 1949	A 1950	S 1951	K 1952	L 1955	D 1956	R 1957	H 1998	D 2017	Y 2018	G 2019	I 2020
MST1	L	M	V	I	Y	C	G	A	V	S	D	G	D	F	G	V
MST2	L	M	V	I	Y	C	G	A	V	S	D	G	D	F	G	V
MST3	I	L	T	I	Y	L	G	G	A	L	D	A	D	F	G	V
MST4	I	L	T	I	Y	L	G	G	A	L	D	A	D	F	G	V

Figure 6. Alignment of key residues in the ATP binding site for LRRK2 and MST kinases. Annotation of binding site residues was based on that described in ref 16. Only binding site residues with differences between LRRK2 and the MST kinases are listed in the table; all others were identical: purple, LRRK2 homology model using TAK-1 kinase as a template; green, corresponding residues from MST3 X-ray crystal structure, PDB code 4U8Z.

Table 3. Key SAR for LRRK2 vs MST Kinases[e]

CMPD	R	LRRK2 IC$_{50}$ (nM)[a]	LRRK2 WCA IC$_{50}$ (nM)[b]	HLM CL (mL/min/Kg)[c]	MST2 IC$_{50}$ (nM)[a]	MST4 IC$_{50}$ (nM)[a]	KSS Selectivity[d]
14		3	25	36	22	178	3/39
32		18	377	48	nt	nt	7/39
33		7	122	53	179	1,099	4/39
34		42	1,331	28	288	6,208	nt
35		5	117	22	196	nt	1/39
36		37	1,467	48	1,333	nt	nt
37		20	390	58	2,388	>32,000	3/39
38		8	133	82	795	12,095	1/39
39		204	nt	63	3,239	9,430	nt
40		111	nt	52	nt	nt	nt
41		2,331	nt	nt	nt	nt	nt
42		139	3,694	57	626	10,218	nt
43		222	3,363	56	nt	nt	nt

[a]Biochemical assay, geometric mean ($n \geq 2$). [b]Cellular assay, geometric mean ($n \geq 2$). [c]Human liver microsomal clearance. [d]Pfizer internal kinase selectivity panel quoted as number of kinases displaying >50% inhibition at 1 μM. [e]nt: not tested.

unsubstituted morpholine **14** but improved MST2 selectivity to 100×. LRRK2 potency did not improve with any of these analogues, which could be due to an increase in desolvation penalty, a conformational entropy penalty due to restricting the flexibility of Arg1957, or due to lack of success in making a productive interaction with the H13 arginine. The X-ray crystal structure of **38** with MST3 (Figure 7) revealed similar
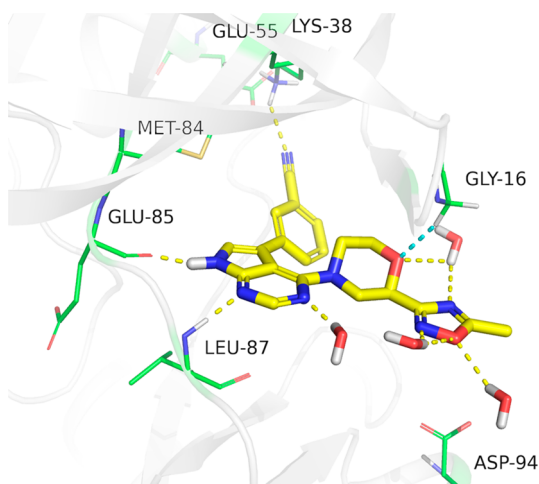
Figure 7. X-ray crystal structure of **38** in MST3 (1.79 Å, PDB code 4W8E).

interactions to those seen with **14**. In addition, the oxadiazole substituent was involved in an intricate water-mediated HB network with the protein. Oxadiazole N4 formed a bifurcated water-mediated HB with the backbone NH of Lys17 in the Gly-rich loop (Asp1887 in LRRK2). This water molecule was also involved in a HB with the morpholine oxygen. O1 in the oxadiazole ring formed a water-mediated HB with Tyr276, a residue that is in an α-helix in an unconserved part of the kinase domain. N2 in the oxadiazole ring was involved in a water-mediated HB network to N3 of the pyrrolopyrimidine core and Tyr86 (Leu1949 in LRRK2), the H5 residue. The MST3 H13 residue, Asp94, is approximately 4.5−5 Å away from the oxadiazole ring, suggesting that the longer Arg1957 in LRRK2 could reach far enough to interact with this substituent.

With the morpholine ring appearing to be key for both potency and selectivity, we also investigated a range of morpholine isosteres (**40−43**); however, all lost significant potency compared to **14** and also to some of the simpler ring systems (e.g., piperidine **9**, pyrrolidine **10**, and azetidine **11**). As the morpholine isosteres are longer and/or orient the oxygen atom differently than the morpholine substituent, this suggested little flexibility in the position of the oxygen atom to make optimal interactions in LRRK2.

As the potency, selectivity, and predicted human pharmacokinetic (PK) properties of **14** were in line with our target profile, we progressed with in vivo experiments to further assess both the potency and pharmacokinetics. The majority of the compounds in this series had passive permeability and P-gp efflux ratios that were suggestive of compounds that should penetrate the blood−brain barrier. Good brain availability in rat, with close to equal distribution across compartments, was observed for **14** (see Supporting Information, Figure S3). However, despite high permeability and moderate clearance, oral bioavailability was poor across species. Clearance in rodent, which was mainly CYP mediated, could be saturated; thus,

appropriate exposure levels could be achieved for initial in vivo studies. Table 4 presents the oral bioavailability data for **14** in the rat, dog, and primate.

Table 4. Oral Pharmacokinetic Data of 14 (5 mg/kg) in Three Species

parameter	units	rat	dog	NHP
C_{max}	ng/mL	181	15	25
T_{max}	h	0.50	0.38	2.0
AUC	ng·h/mL	629	10	78
$t_{1/2}$ (oral)	h	6.22	0.78	2.27
Vd_{ss}	L/kg	1.83	0.92	1.06
F	%	41	0.6	3.5

Despite extensive investigations over many years, there has not yet been a robust model of LRRK2 mediated PD reported in the literature; thus, efficacy measurements currently reflect in vivo LRRK2 inhibition. Compound **14** was dosed to wild type, BAC-transgenic WT LRRK2 and BAC-transgenic G2019S LRRK2 mice. Inhibition was measured by changes in levels of LRRK2 pS935 phosphorylation after compound treatment. Robust dose−response relationships were observed in both brain and kidney in all animals studied. Figure 8 shows the
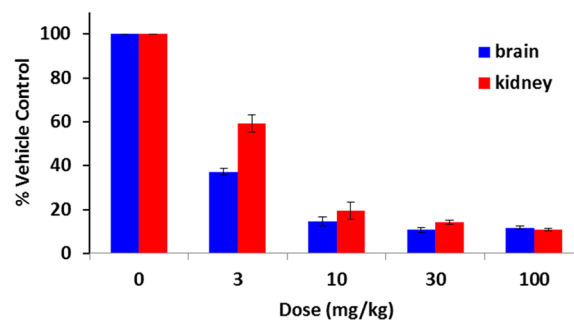
Figure 8. Dose response study of **14** (administered subcutaneously) in wild type mice measuring phosphorylation of S935 in brain and kidney at 90 min after dose (mean ± SEM). Unbound drug IC_{50} values were estimated to be 8 nM in brain and 11 nM in kidney.

results of a representative study in wild-type mice with the unbound drug brain IC_{50} of ∼8 nM corresponding well with the cell-based measurement from ActivX of 15 nM. Total LRRK2 levels were not affected.

Phosphorylation of S935 is not considered to be directly mediated by LRRK2, but rather dephosphorylation of this residue seems to be an indication of inhibitor binding to LRRK2. Recently a LRRK2 autophosphorylation site was identified that may represent a more direct assessment of LRRK2 inhibitor potency.[19] Comparing the inhibition of the two phosphorylation sites by **14** in G2019S mice suggested that pS1292 may represent a somewhat more sensitive measure of LRRK2 inhibition than the pS935 end point (Figure 9). It is also interesting to note that **14** is ∼10× less potent in the BAC-transgenic G2019S mice than WT mice at the pS935 end point.

One of the major concerns regarding chronic LRRK2 administration has been the effects on kidney, where LRRK2 expression is significant. There have been several reports of kidney pathology observed in LRRK2 knock-out (KO) animals, and it has to date been unclear if these effects would be recapitulated by LRRK2 kinase inhibition in adulthood.[20] A number of cell based assays such as THLE cell viability,[21]

H

dx.doi.org/10.1021/jm5014055 | J. Med. Chem. XXXX, XXX, XXX−XXX
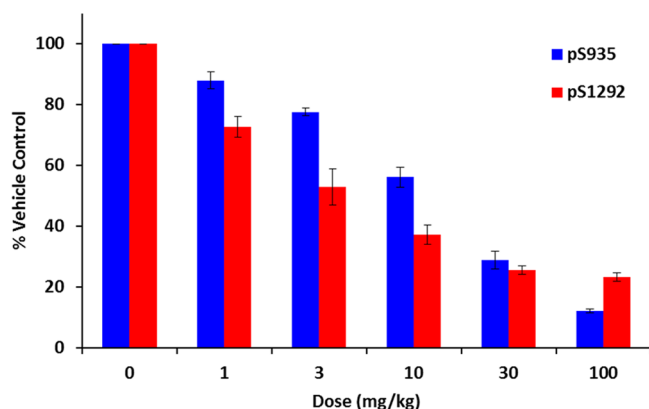
Figure 9. Dose response study of **14** (administered subcutaneously) in G2019S BAC-transgenic mice comparing the response of pS935 and pS1292 phosphorylation to drug treatment in brain lysate (mean ± SEM). IC_{50} values (based on unbound drug concentration) were estimated to be the following: pS935, 103 nM; pS1292, 21 nM.

Ames, and in vitro micronucleus suggested **14** would have a clean safety profile in vivo that would allow assessment of any LRRK2 mediated safety risks. To this end, a 14-day rat exploratory toxicology study was designed to maximize LRRK2 inhibition (target engagement) while minimizing the contribution of off-target kinase inhibition to any safety findings. PK modeling, shown in Figure 10, predicted a b.i.d.-dosing paradigm to give near 24 h coverage of the C_{eff} (set at the unbound drug LRRK2 IC_{50} in brain of 15 nM) at the highest dose. The actual exposures aligned well with the predicted profile and support the maximization of target engagement in conjunction with a blunting of C_{max} exposure. This combination allowed us to better understand the effects of LRRK2 kinase inhibition without the potential for confounding off-target toxicology. As a result, oral administration of **14** twice daily for 15 days was well tolerated at doses up to 60 mg kg^{-1} day^{-1} (31-fold $C_{ave,0-24h}$; 70-fold C_{max}) with only minimal alterations in RBC parameters, electrolytes, and food consumption without concurrent effects on body weight (Table 5). Treated animal kidneys appeared similar to control, as there were no alterations in clinical chemistry or urinary biomarker end points suggesting altered renal function. Additionally, no changes in the lung by routine H&E evaluation and by staining, specifically for type 2 pneumocytes, were noted.[22]

Table 5. Summary of an Oral (b.i.d.) 14-Day Rat Exploratory Toxicology Study at Day 11

dose (mg kg^{-1} day^{-1})	$C_{max,u}$ (nM)	fold C_{eff}	AUC_u (nM·h)	fold C_{eff}	findings
6	86	6	843	2	no treatment related findings
20	380	25	4140	12	no treatment related findings
60	1050	70	11170	31	no treatment related findings

■ CHEMISTRY

The syntheses of analogues **7−43** are illustrated in Scheme 1. Beginning with commercially available **44**, protection of the

Scheme 1. General Synthetic Strategy[a]
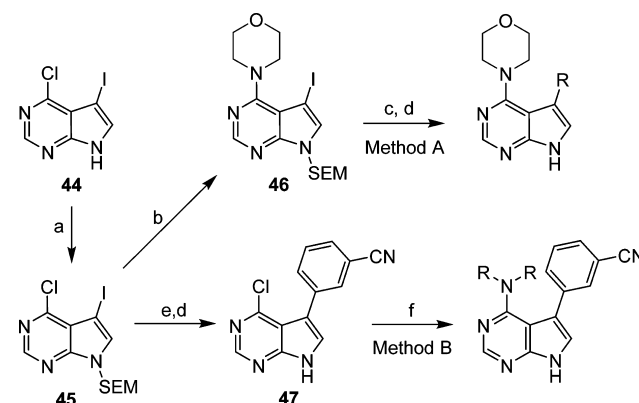
[a]Reagents and conditions: (a) NaH, SEM-Cl, THF, 0 °C; (b) morpholine, DIPEA, *n*-BuOH, reflux; (c) boronic acid/ester, Pd-(dppf)Cl$_2$, K$_2$CO$_3$, EtOH, H$_2$O, Δ; (d) TFA, MeOH (e) (3-cyanophenyl)boronic acid, Pd(dppf)Cl$_2$, K$_2$CO$_3$, DME, H$_2$O, Δ; (f) amine, DIPEA, *n*-BuOH, reflux.

pyrrole N with a SEM group generated **45**. This compound provided access to both points of diversity within the pyrrolopyrimidine scaffold and could be used for single compound preparation or for parallel library compound generation. Suzuki cross-coupling reaction with 3-cyanophenylboronic acid followed by deprotection afforded a key intermediate, **47**. S_NAr displacement of this chloride with amines in either singleton or library format was relatively facile and afforded compounds **7−18**, Table 1. Alternatively, **45** could

Figure 10. Predicted and measured (days 1 and 11) unbound plasma exposures (concentration plasma unbound (Cpu)) following oral dosing (10 and 30 mg/kg b.i.d.) of **14**.

undergo the S_NAr displacement with morpholine to produce **46**. A Suzuki cross-coupling reaction with boronic acids or esters followed by a similar deprotection then produced the compounds shown in Table 2. Where the boronic acids or esters were unstable, **46** could be treated with bis(pinacolato)-diboron under palladium catalysis to produce a stable boronic ester **48** (Scheme 2). With chemistry similar to that shown above, a Suzuki cross-coupling with heterocyclic halides followed by deprotection then yielded the target compounds.
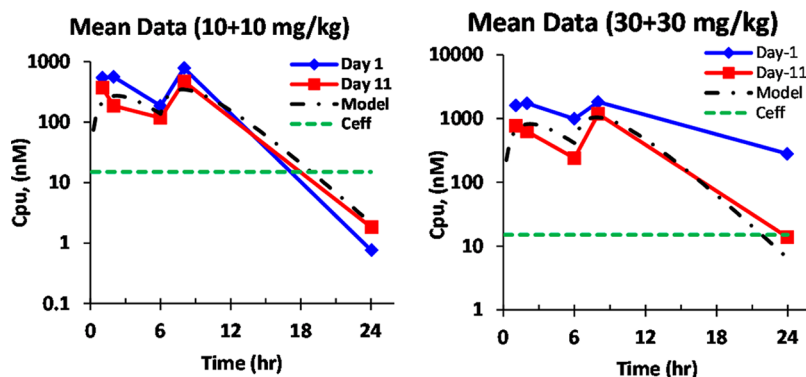
Scheme 2[a]
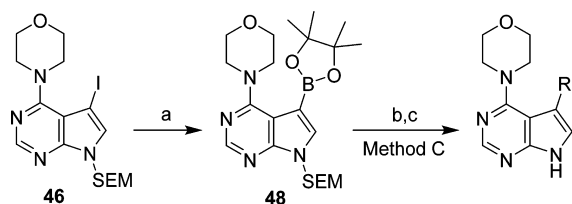
[a]Reagents and conditions: (a) bis(pinacolato)diboron, Pd$_2$(dba)$_3$, XPhos, dioxane, 95 °C; (b) heteroaryl bromide, Pd(PPh$_3$)$_4$, NaHCO$_3$, dioxane/water, 120 °C; (c) TFA, rt.

■ CONCLUSIONS

From a ligand efficient starting point, a series of LRRK2 inhibitors was identified using virtual screening. Optimization, primarily through parallel synthesis, arrived at a potent and selective LRRK2 inhibitor, which is highly brain penetrant. This compound was studied further in rodent pharmacodynamic models, and underwent two-week toxicological assessment. Although the higher species PK is not suitable to continue progression of this compound toward the clinic, its overall properties make this an exceptional tool compound to study the function of LRRK2.

■ EXPERIMENTAL SECTION

Expression and Purification of MST3. Human MST3 kinase domain (residues 1−303; NP_001027467) containing His-tag and thrombin site at the amino terminal region was codon optimized for expression in *E. coli* (BL21-DE3 cells). The protein was purified and crystallized according known published conditions.[23] Briefly, the protein was purified using Ni-NTA metal affinity resin and the purified protein was digested overnight with thrombin (10 U of thrombin/mg protein) to remove the tag, dialyzed against buffer containing 50 mM Tris-HCl (pH 8.0), 100 mM NaCl, and 10% glycerol and concentrated to at least 25 mg/mL.

MST3 Crystallization and Structure Determination. The protein was mixed with 5 mM DTT and 1 mM **14** or **28** or **38** (all prepared as 100 mM stocks in DMSO) and incubated at room temperature for at least an hour. The samples were centrifuged and crystallized by mixing 0.5 μL of the sample with 0.5 μL of the reservoir solution (0.1 M Tris-HCl (pH 8.5), 180 mM MgCl$_2$, 5 mM manganese acetate, and 12−17% PEG3350) using sitting drop vapor-diffusion technique. Crystals were obtained in 1−2 days, and the crystals were frozen in liquid nitrogen using reservoir solution containing 15% glycerol and 1 mM appropriate ligand. 3A7J was used as a search model for determining the structure.

Computational Methods. LRRK2 homology models were constructed with MOE[24] using the AMBER99 force field.[25] The amino acid sequence of human LRRK2 was retrieved from UniProt[26] and aligned to template structures using MOE's Protein Align function with default settings followed by manual editing of loop regions, insertions, and deletions. The template X-ray crystal structures used were TAK-1 (2EVA), MLK1 (3DTC), RET (2IVV), SRC (3DQW), CLK1 (1Z57), and JAK3 (internal structure).

The 10 ns molecular dynamics simulations were run on each homology model using Desmond Suite 2012[27] with the OPLS_2005 force field.[28] The homology models were found to be stable over the course of the simulations with a backbone rmsd of 2.5−3.0 Å from the starting structure after 1 ns. HB interactions of Ser1954 and Asp1956 with Arg1957 were monitored over the course of the simulations.

Biology. LRRK2 Biochemical Assay. LRRK2 kinase activity was measured using Lantha Screen technology from Invitrogen. GST-tagged truncated LRRK2 from Invitrogen (catalog no. PV4874) or mutant G2019S LRRK2 (Invitrogen catalog no. PV4881) was incubated with fluorescein-labeled peptide substrate LRRKtide (Invitrogen catalog no. PR8976A) in the presence of a dose response of compound. Upon completion, the assay was stopped and detected with a terbium labeled anti-phospho-ERM antibody (Invitrogen, catalog no. PR8975A). The assay was carried out under the following protocol: 3 μL of a working solution of substrate (233 nM LRRKtide, 117 μM ATP) prepared in assay buffer (50 mM HEEPES, pH 7.5, 3 mM MgCl$_2$, with 2 mM DTT and 0.01% Brij35 added fresh) was added to a low volume Greiner 384-well plate. The compound dose response was prepared by diluting compound to a top concentration of 3.16 mM in 100% DMSO and serial diluted by half-log in DMSO 11 times. Aliquots (3.5 μL) of the 100% DMSO dose response were mixed with 46.5 μL of water, and then 1 μL of this mixture was added to the 3 μL of substrate mix in the 384-well plate. The kinase reaction was started with 3 μL of a working solution of LRRK2 enzyme at a concentration of 4 μg/mL. The final reaction concentrations were 100 nM LRRKtide, 50 μM ATP, 1.7 μg/mL LRRK2 enzyme, and a compound dose response with a top dose of 32 μM. The reaction was allowed to progress at room temperature for 2 h or 90 min for the mutant protein and then stopped with the addition of 7 μL of detection buffer (20 mM Tris, pH 7.6, 0.01% NP-40, 0.02% NaN$_3$, 6 mM EDTA with 2 nM terbium labeled anti-phospho-ERM). After an incubation of 1 h at room temperature, the plate was read on an Envision with an excitation wavelength of 340 nm and a reading emission at both 520 and 495 nm. The ratio of the 520 and 495 nm emission was used to analyze the data.

Cellular Assay. For transfection and cell treatment, HEK 293 cells were transiently transfected with full length LRRK2 using a DNA/Lipofectamine 2000 ratio of 1:2.5 (μg:μL) in a 85−90% confluent T175 flask. After 6 h the transfection medium was replaced with growth medium (DMEM + 10% FBS) and incubated overnight. The following day cells were harvested and plated into clear tissue culture treated 384-well plates at 10 000 cells/well and allowed to incubate overnight. The next day cells were treated with a dose response of compound for 90 min at 37 °C, 5% CO$_2$. After compound treatment, cells were lysed with 15 μL of lysis buffer (Lantha lysis buffer (Invitrogen, PV5598) with protease inhibitor (Sigma P2714), 0.1% SDS, 1 mM Na$_3$PO$_4$, 17.5 mM Na$_2$H$_2$P$_2$O$_7$, 25 mM NaF, 1 mM PMSF) for 30 min at 4 °C and frozen at −80 °C for 30 min to ensure complete lysis. An amount of 8 μL of the lysed cells was then transferred to ELISA plates coated with LRRK2 capture antibody and blocked with BSA and allowed to incubate overnight at 4 °C.

For ELISA, 384-well high binding plates (Greiner 781074) were coated with 10 μL of mouse monoclonal anti-LRRK2 antibody (Covance SIG-39840) at a final concentration of 10 μg/mL in sodium bicarbonate buffer at pH 9.5 and incubated overnight at 4 °C. Plates were then blocked with 1% BSA in PBS-Tween (0.05%) for 1 h and washed in PBS-Tween before receiving 8 μL of treated cell lysis. The next day plates were washed and incubated with anti-LRRK2 phospho-S935 antibody (Abcam, UDD210(12)) at 1:2000 in PBS-Tween for 1 h and then washed and incubated with an anti-rabbit-HRP antibody (GE Healthcare NA9340V) for 1 h. Plates were washed one final time, and signal was detected with SuperSignal ELISA Pico chemilumines-cent substrate (Pierce 37069).

MST2/4 Biochemical Assay. MST2 and MST4 activity was measured using the Z-Lyte assay kit from Invitrogen (Z-Lyte peptide 7 assay kit, catalog no. PV3180) using MST2 (STK3 catalog no. PV4805) and MST4 (catalog no. PR7067A) supplied from Invitrogen. The assays were run in an assay buffer containing 50 mM HEPES (pH 7.0 for MST2 and pH7.5 for MST4), 0.01% BRIJ-35, 10 mM MgCl$_2$,

and 1 mM EGTA. Compounds were tested in dose response following the kit protocols with the following final assay concentrations; 2 μM Ser/Thr peptide 7, 75 μM ATP, and 18 nM MST2 or MST4. The assay was stopped after 45 min for MST2 and after 60 min for MST4 using the kit stop reagent. Plates were then read using a fluorescence plate reader measuring two emission wavelengths from one excitation wavelength (excitation 400 nm; emission, 445 and 520 nm). Data were analyzed and IC_{50} values determined based on percent phosphorylation calculated from the emission ratio of 445/520 described in the kit protocol.

pS1292 Assay. Custom generated antibody against pS1292 LRRK2 was used. Specificity against pS1292 was verified using pS1292A. Brains and kidneys were homogenized in lysis buffer (50 mM Tris-HCl, pH 7.5, 150 mM NaCl, 1% Triton-X100, 5% glycerol, 10 mM PPA, 20 mM NaF, 2 mM Na_3VO_4, 2 mM EGTA, 2 mM EDTA), incubated on ice for 30 min, and centrifuged at 4 °C for 10 min at 20800g. Supernatant was used for Western blot analysis. Vehicle (1 Mequiv of 1 N HCl, 10% NMP (1-methyl-2-pyrrolidone) in 20% SBECD (β-cyclodextrin sulfobutyl ether) solution) was used as a control.

In Vivo Studies. Four-month-old C57BL/6J or seven-month-old LRRK2 Bac Tg G2910S mice were purchased from JAX Laboratories. All mice were housed on a 12 h light/dark cycle and given free access to food and drinking water as well as environmental enrichment. All animal procedures and animal care methods were approved by Pfizer Institutional Animal Care and Usage Committee. Compound 14 was dissolved in vehicle (10% NMP, 1-methyl-2-pyrrolidone in 20% SBECD, β-cyclodextrin sulfobutyl ether) and subcutaneously administered. Plasma and brain tissues were collected following 90 min of compound administration and snap frozen for further PKPD experiments. Rat studies utilized Wistar Han animals sourced from Charles River Laboratories that were between 200 and 300 g and between 8 and 11 weeks old at study start. For 14, doses were given by oral gavage twice daily for 14 days using a vehicle comprising 10% propylene glycol/20% PEG400/70% 9.5% methocellulose.

Chemistry. General Methods. All solvents and reagents were used as obtained from the commercial vendors. Products were dried under vacuum before being carried on to further reactions or submitted for biological testing. All final products were purified by preparative reverse phase HPLC using appropriate gradients of acetonitrile and water with 0.05% formic acid as the counterion. For syntheses referencing, procedures in other examples or methods reaction conditions (length of reaction and temperature) may vary. Purification conditions may vary between experiments: in general, solvents and the solvent ratios used for eluents/gradients were chosen to provide appropriate R_f or retention times. All tested compounds were determined to be >95% pure by high-performance liquid chromatography under the following conditions. Column: Waters XBridge C18, 2.1 mm × 50 mm, 5 μm. Mobile phase A: 0.0375% trifluoroacetic acid in water. Mobile phase B: 0.01875% trifluoroacetic acid in acetonitrile. Gradient: 1−5% B over 0.60 min, then 5% to 100% B over 3.40 min. Flow rate: 0.8 mL/min. Purity was calculated as a percentage of total area at 254 nm. ^{1}H NMR spectra were recorded on a Bruker instrument operating at 400 MHz. Chemical shifts are expressed in parts per million (ppm, δ) referenced to residual peaks from the deuterated solvents employed (chloroform 7.25 ppm or DMSO-d_6 2.50 ppm). When peak multiplicities are reported, the following abbreviations are used: s = singlet, d = doublet, t = triplet, m = multiplet, br = broad, dd = doublet of doublets, dt = doublet of triplets. Coupling constants are reported in hertz. The mass spectra were obtained using liquid chromatography−mass spectrometry (LC−MS) on an Agilent instrument using atmospheric pressure chemical ionization (APCI) or electrospray ionization (ESI).

4-Chloro-5-iodo-7-((2-(trimethylsilyl)ethoxy)methyl)-7H-pyrrolo[2,3-d]pyrimidine (45). A solution of 4-chloro-5-iodo-7H-pyrrolo[2,3-d]pyrimidine (44) (9.8 g, 35 mmol) in tetrahydrofuran (250 mL) was cooled to 0 °C and treated with sodium hydride (60% in oil, 1.54 g, 38.5 mmol) in three portions. After the reaction mixture had stirred at 0 °C for 1 h, 2-(trimethylsilyl)ethoxymethyl chloride (6.4 g, 38 mmol) was added dropwise, and the reaction mixture was

warmed to room temperature and allowed to stir for 3 h. The reaction was quenched with saturated aqueous sodium chloride solution (250 mL), and the organic layer was dried over sodium sulfate, filtered, and concentrated in vacuo. Silica gel chromatography (eluent, 10:1 petroleum ether/ethyl acetate) afforded the product as a white solid. Yield: 8 g, 20 mmol, 57%. ^{1}H NMR (400 MHz, DMSO-d_6) δ 8.69 (s, 1H), 8.14 (s, 1H), 5.60 (s, 2H), 3.51 (t, J = 8 Hz, 2H), 0.82 (t, J = 8 Hz, 2H), −0.10 (s, 9H).

4-(5-Iodo-7-((2-(trimethylsilyl)ethoxy)methyl)-7H-pyrrolo[2,3-d]pyrimidin-4-yl)morpholine (46). Morpholine (2.45 g, 28.1 mmol) and N,N-diisopropylethylamine (6.63 g, 51.3 mmol) were added to a solution of 4-chloro-5-iodo-7-((2-(trimethylsilyl)ethoxy)methyl)-7H-pyrrolo[2,3-d]pyrimidine (45) (10.5 g, 25.6 mmol) in n-butanol (300 mL), and the reaction mixture was heated at reflux for 18 h, then concentrated under reduced pressure. Aqueous hydrochloric acid (0.1 M, 100 mL) was added and the resulting solid was collected by filtration, washed with water (20 mL), and dried under vacuum to provide the product as a yellow solid. Yield: 8.0 g, 17 mmol, 66%. LCMS m/z 461.2 [M + H$^+$]. ^{1}H NMR (400 MHz, DMSO-d_6) δ 8.39 (s, 1H), 7.81 (s, 1H), 5.52 (s, 2H), 3.80−3.86 (m, 4H), 3.46−3.53 (m, 6H), 0.77−0.84 (m, 2H), −0.10 (s, 9H).

3-(4-Chloro-7H-pyrrolo[2,3-d]pyrimidin-5-yl)benzonitrile (47). *Step 1.* To a stirred mixture of 4-chloro-5-iodo-7-((2-(trimethylsilyl)ethoxy)methyl)-7H-pyrrolo[2,3-d]pyrimidine (45) (8.2 g, 20 mmol), (3-cyanophenyl)boronic acid (3.2 g, 22 mmol), and potassium carbonate (8.3 g, 60 mmol) in a mixture of 1,2-dimethoxyethane and water (4:1 ratio, 250 mL) was added [1,1′-bis(diphenylphosphino)ferrocene]dichloropalladium(II) (731 mg, 1.00 mmol). The reaction mixture was degassed and then charged with nitrogen; this procedure was carried out a total of three times. The reaction mixture was heated at reflux for 3 h, then cooled to room temperature and diluted with saturated aqueous sodium chloride solution (100 mL). The organic layer was dried over sodium sulfate, filtered, and concentrated under reduced pressure. Purification via silica gel column chromatography (eluent, 10:1 petroleum ether/ethyl acetate) provided 3-(4-chloro-7-((2-(trimethylsilyl)ethoxy)methyl)-7H-pyrrolo[2,3-d]pyrimidin-5-yl)benzonitrile as a yellow oil. Yield: 5.0 g, 12 mmol, 60%. ^{1}H NMR (400 MHz, DMSO-d_6) δ 8.75 (s, 1H), 8.13 (s, 1H), 8.00−8.02 (m, 1H), 7.84−7.92 (m, 2H), 7.68 (dd, J = 7.8, 7.8 Hz, 1H), 5.70 (s, 2H), 3.60 (dd, J = 8.0, 8.0 Hz, 2H), 0.86 (dd, J = 8.0, 8.0 Hz, 2H), −0.08 (s, 9H).

Step 2. A solution of 3-(4-chloro-7-((2-(trimethylsilyl)ethoxy)methyl)-7H-pyrrolo[2,3-d]pyrimidin-5-yl)benzonitrile (47) (3.8 g, 9.9 mmol) in trifluoroacetic acid (25 mL) was stirred at room temperature for 2 h. The reaction mixture was concentrated in vacuo and then taken up in methanol (100 mL) and adjusted to pH >12 by addition of solid potassium carbonate. Solvent was removed in vacuo, and the residue was mixed with water (100 mL). The resulting solid was isolated via filtration and washed with water, providing the product as a white solid. Yield: 1.3 g, 5.1 mmol, 52%. ^{1}H NMR (400 MHz, DMSO): δ 13.50−12.50 (bs, 1H), 8.65 (s, 1H), 8.00 (s, 1H), 7.93 (s, 1H), 7.88 (d, J = 7.6 Hz, 1H), 7.82 (d, J = 7.6 Hz, 1H), 7.65 (t, J = 7.8 Hz, 1H). LCMS m/z 255.0 [M + H$^+$].

4-(5-(4,4,5,5-Tetramethyl-1,3,2-dioxaborolan-2-yl)-7-((2-(trimethylsilyl)ethoxy)methyl)-7H-pyrrolo[2,3-d]pyrimidin-4-yl)morpholine (48). To a solution of 4-(5-iodo-7-((2-(trimethylsilyl)ethoxy)methyl)-7H-pyrrolo[2,3-d]pyrimidin-4-yl)morpholine (46) (500 mg, 1.09 mmol) and 4,4,5,5-tetramethyl-1,3,2-dioxaborolane (543 mg, 4.24 mmol) in 1,4-dioxane (20 mL) were added tris(dibenzylideneacetone)dipalladium(0) (99.7 mg, 0.109 mmol), triethylamine (439 mg, 4.34 mmol), and 2-dicyclohexylphosphino-2′,4′,6′-triisopropylbiphenyl (XPhos, 51.8 mg, 0.109 mmol), and the reaction mixture was heated at 95 °C for 18 h. After cooling to room temperature, the reaction mixture was diluted with water (100 mL) and extracted with ethyl acetate (3 × 50 mL). The combined organic layers were washed with saturated aqueous sodium chloride solution (100 mL), dried over sodium sulfate, filtered, and concentrated in vacuo. Purification via silica gel chromatography (gradient, 0−30% ethyl acetate in petroleum ether) afforded the product as a yellow oil. Yield: 415 mg, 0.901 mmol, 83%. LCMS m/z

461.3 [M + H⁺]. ¹H NMR (400 MHz, CDCl₃) δ 8.45 (s, 1H), 7.73 (s, 1H), 5.59 (s, 2H), 3.87−3.93 (m, 4H), 3.68−3.74 (m, 4H), 3.49−3.56 (m, 2H), 1.35 (s, 12H), 0.87−0.93 (m, 2H), −0.06 (s, 9H).

Example of Method A: 5-(1-Methyl-1*H*-pyrazol-4-yl)-4-(morpholin-4-yl)-7*H*-pyrrolo[2,3-*d*]pyrimidine (28).[29] *Step 1.* To a solution of 4-(5-iodo-7-((2-(trimethylsilyl)ethoxy)methyl)-7*H*-pyrrolo[2,3-*d*]pyrimidin-4-yl)morpholine (**46**) (500 mg, 1.1 mmol) and 1-methyl-4-(4,4,5,5-tetramethyl-1,3,2-dioxaborolan-2-yl)-1*H*-pyrazole (272 mg, 1.31 mmol) in a mixture of ethanol and water (4:1, 10 mL) were added dichlorobis(triphenylphosphine)palladium(II) (41 mg, 58 μmol) and potassium carbonate (447 mg, 3.23 mmol). The reaction mixture was degassed and purged with nitrogen; this procedure was carried out a total of three times. It was then heated at 100 °C for 18 h. After concentration in vacuo, the residue was purified via chromatography on silica gel (eluent, 1:1 ethyl acetate/petroleum ether) to provide 4-(5-(1-methyl-1*H*-pyrazol-4-yl)-7-((2-(trimethylsilyl)ethoxy)methyl)-7*H*-pyrrolo[2,3-*d*]pyrimidin-4-yl)-morpholine as a yellow solid. Yield: 200 mg, 0.48 mmol, 44%. ¹H NMR (400 MHz, DMSO-*d₆*) δ 8.39 (s, 1H), 7.86 (s, 1H), 7.59 (s, 1H), 7.52 (s, 1H), 5.57 (s, 2H), 3.90 (s, 3H), 3.50−3.58 (m, 6H), 3.20−3.27 (m, 4H), 0.83 (dd, *J* = 8.0, 7.9 Hz, 2H), −0.09 (s, 9H).

Step 2. A solution of 4-(5-(1-methyl-1*H*-pyrazol-4-yl)-7-((2-(trimethylsilyl)ethoxy)methyl)-7*H*-pyrrolo[2,3-*d*]pyrimidin-4-yl)-morpholine (200 mg, 0.48 mmol) in trifluoroacetic acid (5 mL) was stirred at room temperature for 2 h. The reaction mixture was concentrated under reduced pressure to afford the product as a yellow oil, which was then taken up in methanol (5 mL) and brought to a pH of >12 via addition of solid potassium carbonate. The reaction mixture was stirred for 30 min, filtered, and concentrated in vacuo. Purification via preparative HPLC (column, Agella Venusil ASB C18, 5 μm; mobile phase A, 0.225% formic acid in water; mobile phase B, acetonitrile; eluent, 13% B) provided the product as a yellow solid. Yield: 90 mg, 0.32 mmol, 67%. LCMS *m/z* 285.1 [M + H⁺]. ¹H NMR (400 MHz, DMSO-*d₆*) δ 12.96 (br s, 1H), 8.47 (s, 1H), 7.85 (s, 1H), 7.57 (s, 1H), 7.52 (d, *J* = 2.5 Hz, 1H), 3.90 (s, 3H), 3.53−3.59 (m, 4H), 3.45−3.51 (m, 4H).

Example of Method B: 3-[4-(Morpholin-4-yl)-7*H*-pyrrolo[2,3-*d*]pyrimidin-5-yl]benzonitrile (14).[29] *Step 1.* A solution of 3-(4-chloro-7-((2-(trimethylsilyl)ethoxy)methyl)-7*H*-pyrrolo[2,3-*d*]-pyrimidin-5-yl)benzonitrile (**47**) (3.8 g, 9.9 mmol) in trifluoroacetic acid (25 mL) was stirred at room temperature for 2 h. The reaction mixture was concentrated in vacuo and then taken up in methanol (100 mL) and adjusted to pH >12 by addition of solid potassium carbonate. Solvent was removed in vacuo, and the residue was mixed with water (100 mL). The resulting solid was isolated via filtration and washed with water, providing 3-(4-chloro-7*H*-pyrrolo[2,3-*d*]pyrimidin-5-yl)benzonitrile as a white solid. Yield: 1.3 g, 5.1 mmol, 52%. LCMS *m/z* 255.0 [M + H⁺].

Step 2. Morpholine (871 mg, 10 mmol) and *N,N*-diisopropylethylamine (2.6 g, 20 mmol) were added to a solution of 3-(4-chloro-7*H*-pyrrolo[2,3-*d*]pyrimidin-5-yl)benzonitrile (2.5 g, 9.8 mmol) in *n*-butanol (100 mL), and the reaction mixture was heated at reflux for 3 h. Solvents were removed in vacuo, and the residue was purified using chromatography on silica gel (eluent, 1:1 ethyl acetate/petroleum ether). Subsequent recrystallization from ethyl acetate and *tert*-butyl methyl ether afforded the product as a white solid. Yield: 770 mg, 2.52 mmol, 26%. LCMS *m/z* 306.0 [M + H⁺]. ¹H NMR (400 MHz, DMSO-*d₆*) δ 12.34 (br s, 1H), 8.41 (s, 1H), 7.99−8.02 (m, 1H), 7.89 (br d, *J* = 8 Hz, 1H), 7.76 (br d, *J* = 7.5 Hz, 1H), 7.71 (s, 1H), 7.68 (dd, *J* = 7.8, 7.8 Hz, 1H), 3.44−3.50 (m, 4H), 3.11−3.17 (m, 4H).

Example of Method C. 6-(4-Morpholino-7*H*-pyrrolo[2,3-*d*]pyrimidin-5-yl)picolinonitrile (25). *Step 1.* To a solution of 6-bromopyridine-2-carbonitrile (80 mg, 0.44 mmol) and 4-(5-(4,4,5,5-tetramethyl-1,3,2-dioxaborolan-2-yl)-7-((2-(trimethylsilyl)ethoxy)-methyl)-7*H*-pyrrolo[2,3-*d*]pyrimidin-4-yl)morpholine (**48**) (241 mg, 0.523 mmol) in 1,4-dioxane (2.5 mL) and water (0.5 mL) was added tetrakis(triphenylphosphine)palladium(0) (51 mg, 44 μmol) and sodium carbonate (140 mg, 1.32 mmol). The reaction mixture was heated at 120 °C under microwave irradiation for 15 min, then diluted with water (30 mL) and extracted with ethyl acetate (3 × 50 mL). The

combined organic layers were washed with saturated aqueous sodium chloride solution (100 mL), dried over sodium sulfate, filtered, and concentrated in vacuo; purification via preparative thin layer chromatography (eluent, 1:1 petroleum ether/ethyl acetate) afforded 6-(4-morpholino-7-((2-(trimethylsilyl)ethoxy)methyl)-7*H*-pyrrolo-[2,3-*d*]pyrimidin-5-yl)picolinonitrile as a brown oil. Yield: 110 mg, 0.252 mmol, 57%. ¹H NMR (400 MHz, CDCl₃) δ 8.52 (s, 1H), 7.84−7.93 (m, 2H), 7.74 (s, 1H), 7.59 (dd, *J* = 7.0, 1.2 Hz, 1H), 5.66 (s, 2H), 3.56−3.65 (m, 6H), 3.34−3.40 (m, 4H), 0.93 (dd, *J* = 8.3, 8.0 Hz, 2H), −0.05 (s, 9H).

Step 2. A solution of 6-(4-morpholino-7-((2-(trimethylsilyl)-ethoxy)methyl)-7*H*-pyrrolo[2,3-*d*]pyrimidin-5-yl)picolinonitrile (110 mg, 0.252 mmol) in trifluoroacetic acid (3 mL) was stirred at room temperature for 2 h. The reaction mixture was concentrated in vacuo, taken up in acetonitrile (3 mL), and brought to a pH of >12 via addition of solid potassium carbonate. After 30 min at room temperature, the reaction mixture was filtered and concentrated in vacuo. Purification via preparative HPLC (column, Phenomenex Gemini C18, 8 μm; mobile phase A, ammonia in water, pH 10; mobile phase B, acetonitrile; gradient, 10−50% B) afforded the product as a white solid. Yield: 15.2 mg, 49.6 μmol, 20%. LCMS *m/z* 307.2 [M + H⁺]. ¹H NMR (400 MHz, DMSO-*d₆*) δ 8.38 (s, 1H), 8.13 (dd, *J* = 8.1, 7.7 Hz, 1H), 7.96 (br d, *J* = 8 Hz, 1H), 7.89 (br d, *J* = 8 Hz, 1H), 7.86 (s, 1H), 3.50−3.55 (m, 4H), 3.19−3.24 (m, 4H).

■ ASSOCIATED CONTENT

ⓢ Supporting Information

Experimental details for compounds **7−13**, **15−24**, **26**, **27**, and **29−43c**; figures detailing the tissue exposure (plasma, brain, and kidney) vs time for **14**; tables summarizing kinase selectivity profiles for **12**, **14**, and **28**. This material is available free of charge via the Internet at http://pubs.acs.org.

Accession Codes

PDB codes for MST3 with bound **14** (PF-06447475) is 4U8Z, for **28** (PF-06454589) is 4W8D, and for **38** is 4W8E.

■ AUTHOR INFORMATION

Corresponding Author

*E-mail: paul.galatsis@pfizer.com. Phone: 1-617-326-0709.

Notes

The authors declare no competing financial interest.

■ ABBREVIATIONS USED

BAC, bacterial artificial chromosome; CL, clearance; CNS, central nervous system; Cpu, concentration plasma unbound; CYP, cytochrome P450; ER, efflux ratio; FRET, fluorescence resonance energy transfer; GWAS, genome-wide association studies; HB, H-bond; HLM, human liver microsome; HTS, high throughput screen; JAK, Janus kinase; KO, knock-out; KSS, kinase selectivity screen; LE, ligand efficiency; LipE, lipophilic efficiency; LRRK2, leucine rich repeat kinase 2; MPO, multiparameter optimization; NHP, non-human primate; PBMC, peripheral blood mononuclear cell; PD, Parkinson's disease; PET, positron emission tomography; PFAAT, protein family alignment annotation tool; P-gp, P-glycoprotein; PK, pharmacokinetic; RBC, red blood cell; RLM, rat liver microsome; SEM, 2-(trimethylsilyl)ethoxymethyl; THLE, transformed human liver epithelial cell line; WCA, whole cell assay; WT, wild type; VDW, van der Waals

■ REFERENCES

(1) (a) Lim, K.-L.; Zhang, C. W. Molecular events underlying Parkinson's disease—an interwoven tapestry. *Front. Neurol.* **2013**, *4*, 33. (b) Kurtis, M. M.; Martinez-Martin, P. Parkinson's disease: symptoms, unmet needs and new therapeutic targets. *RSC Drug Discovery* **2013**, *34*, 3−25.

(2) (a) Labbe, C.; Ross, O. A. Association studies of sporadic Parkinson's disease in the genomic era. *Curr. Genomics* **2014**, *15*, 2−10. (b) Lubbe, S.; Morris, H. R. Recent advances in Parkinson's disease genetics. *J. Neurol.* **2014**, *261*, 259−266. (c) Ross, O. A.; Soto-Ortolaza, A. I.; Heckman, M. G.; Aasly, J. O.; Abahuni, N.; Annesi, G.; Bacon, J. A.; Bardien, S.; Bozi, M.; Brice, A.; Brighina, L.; Van Broeckhoven, C.; Carr, J.; Chartier-Harlin, M.-C.; Dardiotis, E.; Dickson, D. W.; Diehl, N. N.; Elbaz, A.; Ferrarese, C.; Ferraris, A.; Fiske, B.; Gibson, J. M.; Gibson, R.; Hadjigeorgiou, G. M.; Hattori, N.; Ioannidis, J. P. A.; Jasinska-Myga, B.; Jeon, B. S.; Kim, Y. J.; Klein, C.; Kruger, R.; Kyratzi, E.; Lesage, S.; Lin, C.-H.; Lynch, T.; Maraganore, D. M.; Mellick, G. D.; Mutez, E.; Nilsson, C.; Opala, G.; Park, S. S.; Puschmann, A.; Quattrone, A.; Sharma, M.; Silburn, P. A.; Sohn, Y. H.; Stefanis, L.; Tadic, V.; Theuns, J.; Tomiyama, H.; Uitti, R. J.; Valente, E. M.; van de Loo, S.; Vassilatis, D. K.; Vilariño-Güell, C.; White, L. R.; Wirdefeldt, K.; Wszolek, Z. K.; Wu, R.-M.; Farrer, M. J. Association of LRRK2 exonic variants with susceptibility to Parkinson's disease: a case-control study. *Lancet Neurol.* **2011**, *10*, 898−908.

(3) (a) Marin, I. The Parkinson disease gene LRRK2: evolutionary and structural insights. *Mol. Biol. Evol.* **2006**, *23*, 2423−2433. (b) Raquel Esteves, A.; Swedlow, R. H.; Cardoso, S. M. LRRK2, a puzzling protein: insights into Parkinson's disease pathogenesis. *Exp. Neurol.* **2014**, *261*, 206−216.

(4) (a) Deng, X.; Dzamko, N.; Prescott, A.; Davies, P.; Liu, Q.; Yang, Q.; Lee, J.-D.; Patricelli, M. P.; Nomanbhoy, T. K.; Alessi, D. R.; Gray, N. S. Characterization of a selective inhibitor of the Parkinson's disease kinase LRRK2. *Nat. Chem. Biol.* **2011**, *7*, 203−205. (b) Ramsden, N.; Perrin, J.; Ren, Z.; Lee, B. D.; Zinn, N.; Dawson, V. L.; Tam, D.; Bova, M.; Lang, M.; Drewes, G.; Bantscheff, M.; Bard, F.; Dawson, T. M.; Hopf, C. Chemoproteomics-based design of potent LRRK2-selective lead compounds that attenuate Parkinson's disease-related toxicity in human neurons. *ACS Chem. Biol.* **2011**, *6*, 1021−1028. (c) Reith, A. D.; Bamborough, P.; Jandu, K.; Andreotti, D.; Mensah, L.; Dossang, P.; Choi, H. G.; Deng, X.; Zhang, J.; Alessi, D. R.; Gray, N. S. GSK2578215A; a potent and highly selective 2-arylmethoxy-5-substituent-*N*-arylbenzamide LRRK2 kinase inhibitor. *Bioorg. Med. Chem. Lett.* **2012**, *22*, 5625−5630. (d) Estrada, A. A.; Liu, X.; Baker-Glenn, C.; Beresford, A.; Burdick, D. J.; Chambers, M.; Chan, B. K.; Chen, H.; Ding, X.; DiPasquale, A. G.; Dominguez, S. L.; Dotson, J.; Drummond, J.; Flagella, M.; Flynn, S.; Fuji, R.; Gill, A.; Gunzner-Toste, J.; Harris, S. F.; Heffron, T. P.; Kleinheinz, T.; Lee, D. W.; Le Pichon, C. E.; Lyssikatos, J. P.; Medhurst, A. D.; Moffat, J. G.; Mukund, S.; Nash, K.; Scearce-Levie, K.; Sheng, Z.; Shore, D. G.; Tran, T.; Trivedi, N.; Wang, S.; Zhang, S.; Zhang, X.; Zhao, G.; Zhu, H.; Sweeney, Z. K. Discovery of highly potent, selective, and brain-penetrable leucine-rich repeat kinase 2 (LRRK2) small molecule inhibitors. *J. Med. Chem.* **2012**, *55*, 9416−9433. (e) Galatsis, P.; Henderson, J. L.; Kormos, B. L.; Han, S.; Kurumbail, R. G.; Wager, T. T.; Verhoest, P. R.; Noell, G. S.; Chen, Y.; Needle, E.; Berger, Z.; Steyn, S. J.; Houle, C.; Hirst, W. D. Kinase domain inhibition of leucine rich repeat kinase 2 (LRRK2) using a [1,2,4]triazolo[4,3-*b*]pyridazine scaffold. *Bioorg. Med. Chem. Lett.* **2014**, *24*, 4132−4140.

(5) Wager, T. T.; Hou, X.; Verhoest, P. R.; Villalobos, A. Moving beyond rules: the development of a central nervous system multiparameter optimization (CNS MPO) approach to enable alignment of druglike properties. *ACS Chem. Neurosci.* **2010**, *1*, 435−449.

(6) (a) Manning, G.; Whyte, D. B.; Martinez, R.; Hunter, T.; Sudarsanam, S. The protein kinase complement of the human genome. *Science* **2002**, *298*, 1912−1934. (b) Zhang, D.; Lin, J.; Han, J. Receptor-interacting protein (RIP) kinase family. *Cell. Mol. Immunol.* **2010**, *7*, 243−249.

(7) Xi, H.; Lunney, E. A. The design, annotation, and application of a kinase-targeted library. In *Chemical Library Design*; Zhou, J. Z., Ed.; Methods in Molecular Biology, Vol. *685*; Humana Press: New York, 2011; pp 279−291.

(8) Caffrey, D. R.; Dana, P. H.; Mathur, V.; Ocano, M.; Hong, E.-J.; Wang, Y. E.; Somaroo, S.; Caffrey, B. E.; Potluri, S.; Huang, E. S. PFAAT version 2.0: a tool for editing, annotating, and analyzing multiple sequence alignments. *BMC Bioinf.* **2007**, *8*, 381.

(9) Carhart, R. E.; Smith, D. H.; Venkataraghavan, R. Atom pairs as molecular features in structure−activity studies: definition and applications. *J. Chem. Inf. Comput. Sci.* **1985**, *25*, 64−73.

(10) (a) Rarey, M.; Dixon, J. S. Feature trees: a new molecular similarity measure based on tree matching. *J. Comput.-Aided Mol. Des.* **1998**, *12*, 471−490. (b) Rarey, M.; Hindle, S.; Maass, P.; Metz, G.; Rummey, C.; Zimmermann, M. Feature trees: theory and applications from large-scale virtual screening to data analysis. In *Pharmacophores and Pharmacophore Searches*; Langer, T., Hoffman, R. D., Eds.; Methods and Principles in Medicinal Chemistry, Vol. *32*; Wiley-VCH: Weinheim, Germany, 2006; pp 81116

(11) Chen, H.; Chan, B. K.; Drummond, J.; Estrada, A. A.; Gunzner-Toste, J.; Liu, X.; Liu, Y.; Moffat, J.; Shore, D.; Sweeney, Z. K.; Tran, T.; Wang, S.; Zhao, G.; Zhu, H.; Burdick, D. J. Discovery of selective LRRK2 inhibitors guided by computational analysis and molecular modeling. *J. Med. Chem.* **2012**, *55*, 5536−5545.

(12) Delbroek, L.; Van Kolen, K.; Steegmans, L.; da Cunha, R.; Mandemakers, W.; Daneels, G.; De Bock, P.-J.; Zhang, J.; Gevaert, K.; De Strooper, B.; Alessi, D. R.; Verstreken, P.; Moechars, D. W. Development of an enzyme-linked immunosorbent assay for detection of cellular and in vivo LRRK2 S935 phosphorylation. *J. Pharm. Biomed. Anal.* **2013**, *76*, 49−58.

(13) Graves, L. M.; Litchfield, D. W. "Going KiNativ": probing the native kinome. *Chem. Biol.* **2011**, *18*, 683−684.

(14) (a) Troxler, T.; Greenidge, P.; Zimmermann, K.; Desrayaud, S.; Druckes, P.; Schweizer, T.; Stauffer, D.; Rovelli, G.; Shimshek, D. R. Discovery of novel indolinone-based, potent, selective and brain penetrant inhibitors of LRRK2. *Bioorg. Med. Chem. Lett.* **2013**, *23*, 4085−4090. (b) Mologni, L.; Rostagno, R.; Brussolo, S.; Knowles, P. P.; Kjaer, S.; Murray-Rust, J.; Rosso, E.; Zambon, A.; Scapozza, L.; McDonald, N. Q.; Lucchini, V.; Gambacorti-Passerini, C. Synthesis, structure−activity relationship and crystallographic studies of 3-substituted indolin-2-one RET inhibitors. *Bioorg. Med. Chem.* **2010**, *18*, 1482−1496. (c) Sun, L.; Tran, N.; Tang, F.; App, H.; Hirth, P.; McMahon, G.; Tang, C. Synthesis and biological evaluations of 3-substituted indolin-2-ones: a novel class of tyrosine kinase inhibitors that exhibit selectivity toward particular receptor tyrosine kinases. *J. Med. Chem.* **1998**, *41*, 2588−2603.

(15) Radu, M.; Chernoff, J. The DeMSTification of mammalian ste20 kinases. *Curr. Biol.* **2009**, *19*, R421−R425.

(16) Xing, L.; Rai, B.; Lunney, E. A. Scaffold mining of kinase hinge binders in crystal structure database. *J. Comput.-Aided Mol. Des.* **2014**, *28*, 13−23.

(17) (a) Chan, B. K.; Estrada, A. A.; Chen, H.; Atherall, J.; Baker-Glenn, C.; Beresford, A.; Burdick, D. J.; Chambers, M.; Dominguez, S. L.; Drummond, J.; Gill, A.; Kleinheinz, T.; Le Pichon, C. E.; Medhurst, A. D.; Liu, X.; Moffat, J. G.; Nash, K.; Scearce-Levie, K.; Sheng, Z.; Shore, D. G.; Van de Poel, H.; Zhang, S.; Zhu, H.; Sweeney, Z. K. Discovery of a highly selective, brain-penetrant aminopyrazole LRRK2 inhibitor. *ACS Med. Chem. Lett.* **2013**, *4*, 85−90. (b) Estrada, A. A.; Chan, B. K.; Baker-Glenn, C.; Beresford, A.; Burdick, D. J.; Chambers, M.; Chen, H.; Dominguez, S. L.; Dotson, J.; Drummond, J.; Flagella, M.; Fuji, R.; Gill, A.; Halladay, J.; Harris, S. F.; Heffron, T. P.; Kleinheinz, T.; Lee, D. W.; Pichon, C. E. L.; Liu, X.; Lyssikatos, J. P.; Medhurst, A. D.; Moffat, J. G.; Nash, K.; Scearce-Levie, K.; Sheng, Z.; Shore, D. G.; Wong, S.; Zhang, S.; Zhang, X.; Zhu, H.; Sweeney, Z. K. Discovery of highly potent, selective, and brain-penetrant amino-pyrazole leucine-rich repeat kinase 2 (LRRK2) small molecule inhibitors. *J. Med. Chem.* **2014**, *57*, 921−936.

(18) (a) Bertrand, J. A.; Thieffine, S.; Vulpetti, A.; Cristiani, C.; Valsasina, B.; Knapp, S.; Kalisz, H. M.; Flocco, M. Structural

characterization of the GSK-3β active site using selective and non-selective ATP-mimetic inhibitors. *J. Mol. Biol.* **2003**, *333*, 393−407. (b) Bhat, R.; Xue, Y.; Berg, S.; Hellberg, S.; Ormö, M.; Nilsson, Y.; Radesäter, A.-C.; Jerning, E.; Markgren, P.-O.; Borgegård, T.; Nylöf, M.; Giménez-Cassina, A.; Hernández, F.; Lucas, J. J.; Díaz-Nido, J.; Avila, J. Structural insights and biological effects of glycogen synthase kinase 3-specific inhibitor AR-A014418. *J. Biol. Chem.* **2003**, *278*, 45937−45945.

(19) Sheng, Z.; Zhang, S.; Bustos, D.; Kleinheinz, T.; Le Pichon, C. E.; Dominguez, S. L.; Solanoy, H. O.; Drummond, J.; Zhang, X.; Ding, X.; Cai, F.; Song, Q.; Li, X.; Yue, Z.; van der Brug, M. P.; Burdick, D. J.; Gunzner-Toste, J.; Chen, H.; Liu, X.; Estrada, A. A.; Sweeney, Z. K.; Scearce-Levie, K.; Moffat, J. G.; Kirkpatrick, D. S.; Zhu, H. Ser1292 autophosphorylation is an indicator of LRRK2 kinase activity and contributes to the cellular effects of PD mutations. *Sci. Transl. Med.* **2012**, *4*, 164ra161.

(20) (a) Ness, D.; Ren, Z.; AGardai, S.; Sharpnack, D.; Johnson, V. J.; Brennan, R. J.; Brigham, E. F.; Olaharski, A. J. Leucine-rich repeat kinase 2 (LRRK2)-deficient rats exhibit renal tubule injury and perturbations in metabolic and immunological homeostasis. *PLoS One* **2013**, *8*, e66164. (b) Herzig, M. C.; Kolly, C.; Persohn, E.; Theil, D.; Schweizer, T.; Hafner, T.; Stemmelen, C.; Troxler, T. J.; Schmid, P.; Danner, S.; Schnell, C. R.; Mueller, M.; Kinzel, B.; Grevot, A.; Bolognani, F.; Stirn, M.; Kuhn, R. R.; Kaupmann, K.; van der Putten, P. H.; Rovelli, G.; Shimshek, D. R. LRRK2 protein levels are determined by kinase function and are crucial for kidney and lung homeostasis in mice. *Hum. Mol. Genet.* **2011**, *20*, 4209−4223. (c) Tong, Y.; Yamaguchi, H.; Giaime, E.; Boyle, S.; Kopan, R.; Kelleher Raymond, J., 3rd; Shen, J. Loss of leucine-rich repeat kinase 2 causes impairment of protein degradation pathways, accumulation of alpha-synuclein, and apoptotic cell death in aged mice. *Proc. Natl. Acad. Sci. U.S.A.* **2010**, *107*, 9879−9884.

(21) Greene, N.; Aleo, M. D.; Louise-May, S.; Price, D. A.; Will, Y. Using an in vitro cytotoxicity assay to aid in compound selection for in vivo safety studies. *Bioorg. Med. Chem. Lett.* **2010**, *20*, 5308−5312.

(22) Fuji, R. Nonclinical safety studies of selective LRRK2 kinase inhibitors. Presented at Seventh Annual Parkinson's Disease Therapeutics Conference, The New York Academy of Sciences, October 24, 2013.

(23) Ko, T. P.; Jeng, W. Y.; Liu, C. I.; Lai, M. D.; Wu, C. L.; Chang, W. J.; Shr, H. L.; Lu, T. J.; Wang, A. H. J. Structures of human MST3 kinase in complex with adenine, ADP, an dMn2+. *Acta Crystallogr.* **2010**, *66*, 145−154.

(24) *Molecular Operating Environment (MOE)*, version 2013.08; Chemical Computing Group Inc. (1010 Sherbooke St. West, Suite No. 910, Montreal, QC, H3A 2R7, Canada), 2013.

(25) Wang, J.; Cieplak, P.; Kollman, P. A. How well does a restrained electrostatic potential (RESP) model perform in calculating conformational energies of organic and biological molecules? *J. Comput. Chem.* **2000**, *21*, 1049−1074.

(26) The Universal Protein Resource (UniProt). *Nucleic Acids Res.* **2008**, *36*, D190−D195.

(27) (a) *Desmond Molecular Dynamics System*, version 3.1; D. E. Shaw Research: New York, NY, 2012. (b) *Maestro-Desmond Interoperability Tools*, version 3.1; Schrödinger: New York, NY, 2012. (c) Bowers, K. J.; Chow, E.; Xu, H.; Dror, R. O.; Eastwood, M. P.; Gregersen, B. A.; Klepeis, J. L.; Kolossvary, I.; Moraes, M. A.; Sacerdoti, F. D.; Salmon, J. K.; Shan, Y.; Shaw, D. E. Scalable algorithms for molecular dynamics simulations on commodity clusters. *Proceedings of the ACM/IEEE Conference on Supercomputing (SC06)*, Tampa, FL, , November 11−17, 2006; ACM Press: New York, 2006.

(28) Banks, J. L.; Beard, H. S.; Cao, Y.; Cho, A. E.; Damm, W.; Farid, R.; Felts, A. K.; Halgren, T. A.; Mainz, D. T.; Maple, J. R.; Murphy, R.; Philipp, D. M.; Repasky, M. P.; Zhang, L. Y.; Berne, B. J.; Friesner, R. A.; Gallicchio, E.; Levy, R. M. Integrated modeling program, applied chemical theory (IMPACT). *J. Comput. Chem.* **2005**, *26*, 1752−1780.

(29) Compounds **14** (PF-06447475) and **28** (PF-06454589) are now available from Sigma Aldrich.